Macroscopic consequences of Piobert–Lüders and Portevin–Le Chatelier bands during tensile deformation in Al-Mg alloys

Baptiste Reyne, Pierre-Yves Manach, Nicolas Moes

Macroscopic consequences of Piobert–Lüders and Portevin–Le Chatelier bands during tensile deformation in Al-Mg alloys

Baptiste Reyne[a,b,*], Pierre-Yves Manach[b], Nicolas Moës[a]

[a] *Centrale Nantes, UMR CNRS 6183, GeM, 1 rue de la Noë, 44321 Nantes Cedex 3, France*
[b] *Univ. Bretagne Sud, UMR CNRS 6027, IRDL, F-56100 Lorient, France*

Abstract

Lüders bands and the Portevin–Le Chatelier effect are both due to plastic flow instabilities that affect a wide variety of metallic materials. The present study focuses on understanding these behaviors. Field kinematic measurements combined with the comparison of two specimen sizes are used here to characterize the Al–Mg alloy AA5086, by investigating the kinetics of individual localization bands. A unifying point of view is proposed for the classification of these bands together with the identification of a constitutive relation linking strain increments and nucleation stress, as well as evidence of the factors determining the development of serration behaviors. This leads to a novel interpretation of the spatiotemporal behavior of the bands as being the result of a competition between the influence of plastic strain and its gradient.

Keywords: characterization, aluminium alloys, plasticity, Portevin–Le Chatelier, Piobert–Lüders, strain localization

1. Introduction

At the onset of plastic yielding, a wide variety of metallic materials develop Piobert-Lüders (PL) bands [1, 2] associated with a peak in stress and a plateau on the hardening curves. Among these materials, some impure alloys subsequently exhibit the Portevin–Le Chatelier (PLC) effect [3, 4], which is an irregular hardening (or jerky plastic flow) combining stress drops (serrations) with a negative strain rate sensitivity (NSRS). The common feature of both of these behaviors is a heterogeneous plastic flow under an apparently homogeneous stress: thin localization bands, which are often described as propagating, serve to spread increments of plastic strain over the material domain. It is commonly accepted that PL bands and the PLC effect arise from strain aging micro-mechanisms associated with the pinning of dislocations by solutes [5]. For instance, in the case of PLC in Al-Mg alloys, the diffusion of magnesium solutes enables the repetition of pinning leading to dynamic strain aging (DSA) [6, 7] as opposed to static strain aging (SSA) for PL bands [8].

*Corresponding author.
Email addresses: baptiste.reyne@ec-nantes.fr (Baptiste Reyne), pierre-yves.manach@univ-ubs.fr (Pierre-Yves Manach), nicolas.moes@ec-nantes.fr (Nicolas Moës)

Three types of PLC behavior are classically distinguished [9] depending on temperature, plastic strain magnitude and strain rate, in addition to the material micro-structure. At high strain rates and low temperatures, type A bands nucleate smoothly and in spatial order associated with Lüders-like peak stress and plateaus. At low strain rates and high temperatures, type C bands grow in an uncorrelated manner [10, 11] and strong serrations are observed. An intermediate situation corresponds to type B, often referred to as *hopping* bands, which are spatially ordered but come with distinct stress drops. For both types B and C, it has been established that the nucleation of each band occurs along with a single serration [12]. This classification of plastic instabilities in discrete categories poses a problem for the interpretation of transition and crossover regimes which remains to be resolved [13]. In the following, this issue is tackled by suggesting a continuum that allows for a smooth evolution from one type to another.

The quantitative assessment of plastic instabilities is mostly performed using tensile tests although recent investigations extend the technique to additional loading paths, such as simple shear [14, 15], biaxial expansion [16] or equi-biaxial deformation [17]. In addition to stress drop distributions, the characterization of PL bands and the PLC effect essentially relies on specific kinematic measures. The band morphology of softening material is a common topic of research in the literature; the orientation of bands remains constant throughout tensile tests [18, 19] while their width exhibits a positive strain rate sensitivity [10, 20, 21, 19]. Although the deformation mode has been rarely investigated in detail, it is known to correspond principally to simple shear[19]. The strain increment carried by bands is found to increase monotonically with strain [22, 23] sometimes with a linear trend [24, 25] and sensitive to strain rate [26, 27]. Finally, the apparent velocity of bands propagation have been measured in several studies [28, 29, 30, 27, 31] and understood to accommodate the imposed kinematics [32], as explained in section 3.2. While existing studies provide extensive information on the macroscopic kinematics aspects, interpretation of the results can be hindered by the scarcity of data points caused by the difficulty of their assessment, as well as the need to cover a wide range of parameter variability. Since sample size is one of the relevant parameters whose influence on PL and PLC bands remains to be thoroughly investigated, this aspect is addressed in the present study. To develop novel and original approaches, in addition to investigating the phenomenology, specialists in modeling and simulation require experimental studies and conceptual tools for validation and analysis at the scale of industrial application.

Apart from dealing with questions on the microscopic mechanisms governing the PLC effect, this study aims to provide a global and coherent view on their macroscopic consequences that may be useful for new modeling approaches of this effect. For this purpose, tensile tests are performed on an Al–Mg alloy at room temperature over a wide range of imposed strain rates. By comparing two different sizes of samples, the analysis can be focused on the width of a band and explore the intrinsic nature of the usual variables of interest. The information thus obtained enables us to draw conclusions about the behavior of PL and PLC bands as macroscopic mechanical objects.

2. Experiments

2.1. Material

Experiments are conducted on rolled sheets of aluminum-magnesium alloy (AA5086-H111) with a nominal thickness of 0.8 mm (a thorough thermo-mechanical characterization of this material is available in [33]). The chemical compound are semi-quantitatively evaluated using scanning electron microscopy and energy-dispersive X-ray spectroscopy (EDS) on eight samples. They report 95.5(5) % aluminum and 4.5(5) % magnesium.

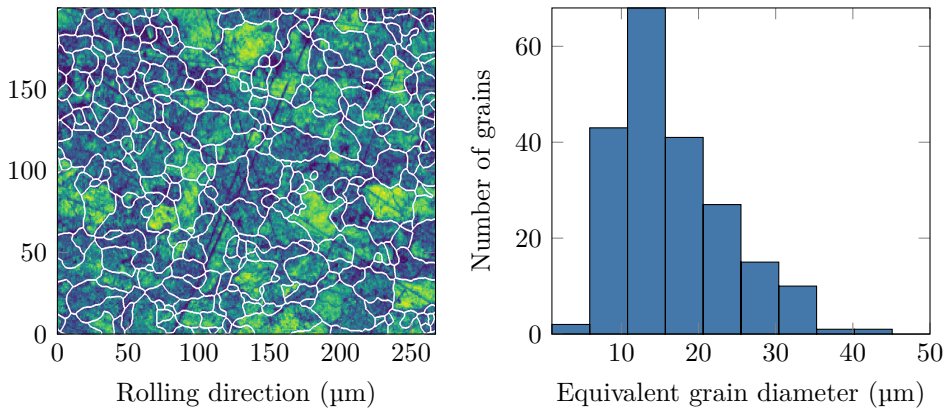

Figure 1: Electron backscatter diffraction results on AA5086 post-treated with the MTEX [34] toolbox. The computed grains boundaries are superimposed with bands contrast on fig. 1a. Figure 1b gives a histogram of the grains equivalent diameters.

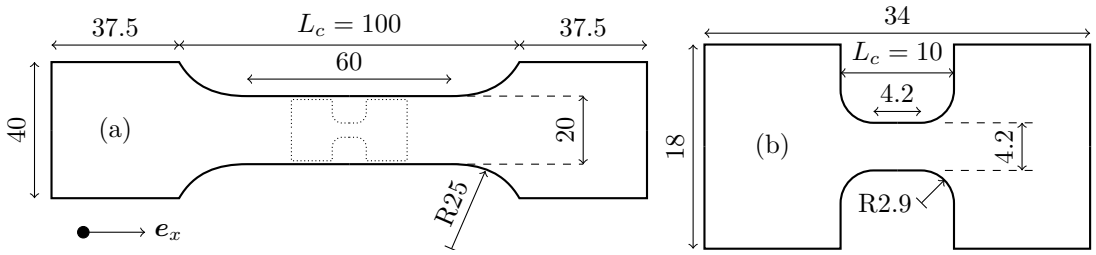

Figure 2: Geometries referred to as *large* (2a) and *small* (2b). Dimensions are given in mm.

Figure 1 provides insights on the material micro-structure using electron backscatter diffraction (EBSD). Measurements are conducted on polished samples before and after deformation, then post-treated with the MTEX library [34]. The average grain diameter is 16 µm. The material texture exhibits no notable anisotropy on any sample in spite of the rolled sheet forming process and applied deformation.

2.2. Experimental procedure

Two sets of tensile tests associated with distinct samples geometries and corresponding test apparatus are considered as illustrated in fig. 2. They are both cut using electrical discharge machining and kept at room temperature. Medium-size measurements are performed with a conventional geometry referred to as *large* (fig. 2a) tested with a Instron tensile machine using a 10 kN load cell. Results from smaller-sized specimens, referred to here as *small* samples (fig. 2b) allow us to distinguish the geometry effects from the material influence and to isolate the phenomenon at the scale of a band. Small samples are tested with both an Instron-10 kN and a MicroTest machine using a 2 kN cell to improve the accuracy of the force measurements under the lowest strain rates. This geometry is based on the study of [35] and [27] who characterized AA5754 at an identical scale by means of thermal radiation and strain gauge measurements.

All tensile tests are performed with the rolling direction aligned with the cross-head displacement, defining the axial basis vector $\boldsymbol{e}_x$ in fig. 2. After setting the sample in the device, the grips are closed, thus inducing a pre-stress that is kept within the material elastic domain. A constant

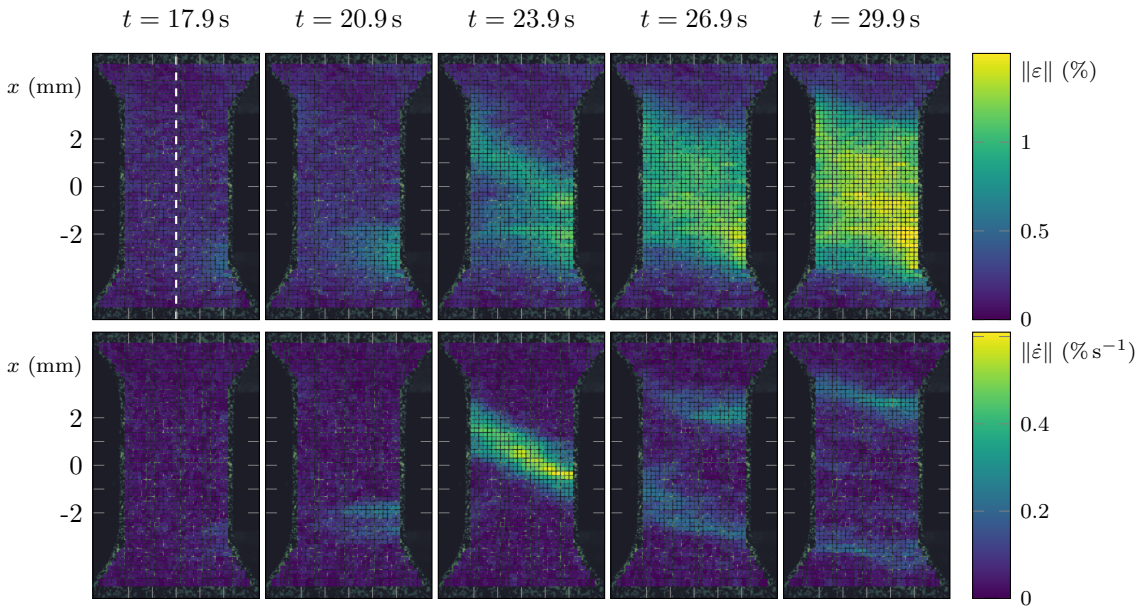

Figure 3: Snapshots of the strain norm (upper row) and strain rate norm (bottom row) for a small sample at nominal strain rate $v_c/L_c = 6.67 \times 10^{-4}\,\mathrm{s}^{-1}$ during PL band nucleation and propagation. Each square represents a finite element used for DIC.

velocity denoted v_c is then applied to the mobile cross-head until fracture of the sample. Each geometry is characterized by the initial length of its gauge zone L (60 mm large and 4.2 mm small) and by the initial total length between grips L_c (100 mm for large and 10 mm for small). The specimens are tested at room temperature with several constant imposed velocities and a ratio v_c/L_c, referred to as the *nominal strain rate*, covering an interval from $10^{-4}\,\mathrm{s}^{-1}$ to $10^{-1}\,\mathrm{s}^{-1}$.

Samples are prepared with a random black and white painted pattern; a camera (100 mm macro lens) is set and adjusted in front of the sample. The tensile force signal is acquired and synchronized with images taken at a common variable rate ranging from 3 fps to 240 fps, which enables intermittent temporal refinements for the analysis of subtle events. Data gathering process and optical equipment are both managed with the Aramis system (Gom, Germany).

2.3. Post-processing

Displacement fields are computed from pictures using digital image correlation (DIC) and the dedicated software `UFreckles`[36] that outputs measurements in the `Matlab` matrix format. The images are discretized with ordered Q4 finite elements, allowing fields to be approximated as shown in fig. 3. The physical elements size varies from 130 µm to 200 µm for small samples and from 550 µm to 700 µm for large samples. For 1D studies, the results are gathered together on the line of nodes that is the closest to the axis of symmetry drawn as dashed lines on the upper-left graph. Gradients and rates are then computed by means of finite differences.

The Cauchy stress is assumed homogeneous over the gauge area in order to compare both geometries. It is taken equal to $\sigma \boldsymbol{e}_x \otimes \boldsymbol{e}_x$ with $\sigma = F/A$ where F is the output force signal and A is the current cross-sectional area, computed using the assumption of small strains and isochoric deformation from DIC strain results. Contrarily, the strain field and its rate are strongly heterogeneous due to the occurrence of PL bands and the PLC effect, imposing a distinction between the global

nominal strain u_c/L_c and local measures (where u_c is the cross-head displacement). Moreover, it can be observed that the actual gauge zone elongation rate v/L (where v is the elongation rate of the gauge zone and L its length) is strongly sensitive to geometry and cumulative plastic strain: in the case of small samples, it diverges by up to 75 % from the nominal strain rate (averaged values can be compared in table 1a). Hence, it should be considered as an order of magnitude over the gauge area, which is only used as a test label. The local strain $\boldsymbol{\varepsilon}$ is computed as the linearized Green-Lagrange measure from digital image correlation.

2.4. Overview of one-dimensional graphical representations

Figure 4 shows a propagating behavior associated with the so called type A kinetics—different nominal strain rates are analyzed in section 3.4. Figures 4a and 4c display the local stress vs. time and the local stress vs. strain, respectively. It should be noted that the virtual gauge zone, shown on the right hand side figures and centered at 43 mm, would have yield different values if taken elsewhere, as the strain at a given instant is uneven over the studied domain.

Figure 4b is the *characteristic* representation where the strain rate magnitude is mapped as a function of time along the axis of interest. This representation is widely used in the context of propagating waves and is applied to characterizing the PLC effect by means of acoustic emissions and laser extensometry [11], infrared radiation [29, 35] or kinematic fields [30]; and used by [37] to develop a numerical tool for band detection in finite element simulations. The dark patterns reflect an intense strain activity and correspond to the band location at each given instant. The numerical evaluation of the local strain rate requires the numerical derivation of the displacement field in both space and time. This latter step involves large uncertainties due to the varying acquisition frequency which, in the absence of quantitative information, justifies the normalization of strain rate magnitudes.

Figure 4d shows the *kinematic* representation partially used in [24]: it consists of all the spatial strain distributions measured during the full range of the test, plotted successively as dotted lines. The time difference between each plot shown here is constant and equal to 4.17 µs, corresponding to the camera acquisition frequency. Had the strain remained homogeneous, only horizontal lines would be displayed. When a strain state persists in time, several lines become superimposed, yielding a thicker cluster of lines. On the contrary, transient states only occupy a space of the graph once. As a result, the kinematic behavior of the bands can be directly visualized. Even though time is not explicitly indicated, the variation of local axial strain with time can be understood due to the fact that strain at any given point can only increase since the deformation is essentially plastic and the test is monotonic. Then, for any given line, the subsequent state is represented by the line directly above. Using such a representation, the quality and quantity of the strain jump carried by each band can be assessed by looking at the difference between two persistent states; and its location evaluated graphically as detailed in section 3.2.

The first occurrence of Lüders bands (pointers p1) is associated with the spreading of a uniform strain increment (pointer p2) over the initially homogeneous distribution. Nucleation occurs at each extremity of the sample and a propagation trend continues until coalescence (pointer p3) at $x \approx 42$ mm. Then the PLC effect takes over with several increments of increasing amplitude. The zone ($x \in [40; 55]$mm) where strain increments are seen to override each other in an irregular way coincides with a change in band orientation; this behavior is observed in most tests. The inherent nature of the strain increment in characterizing the PLC effect is clearly expressed here since the heterogeneities are maintained and enhanced after the onset of band growth.

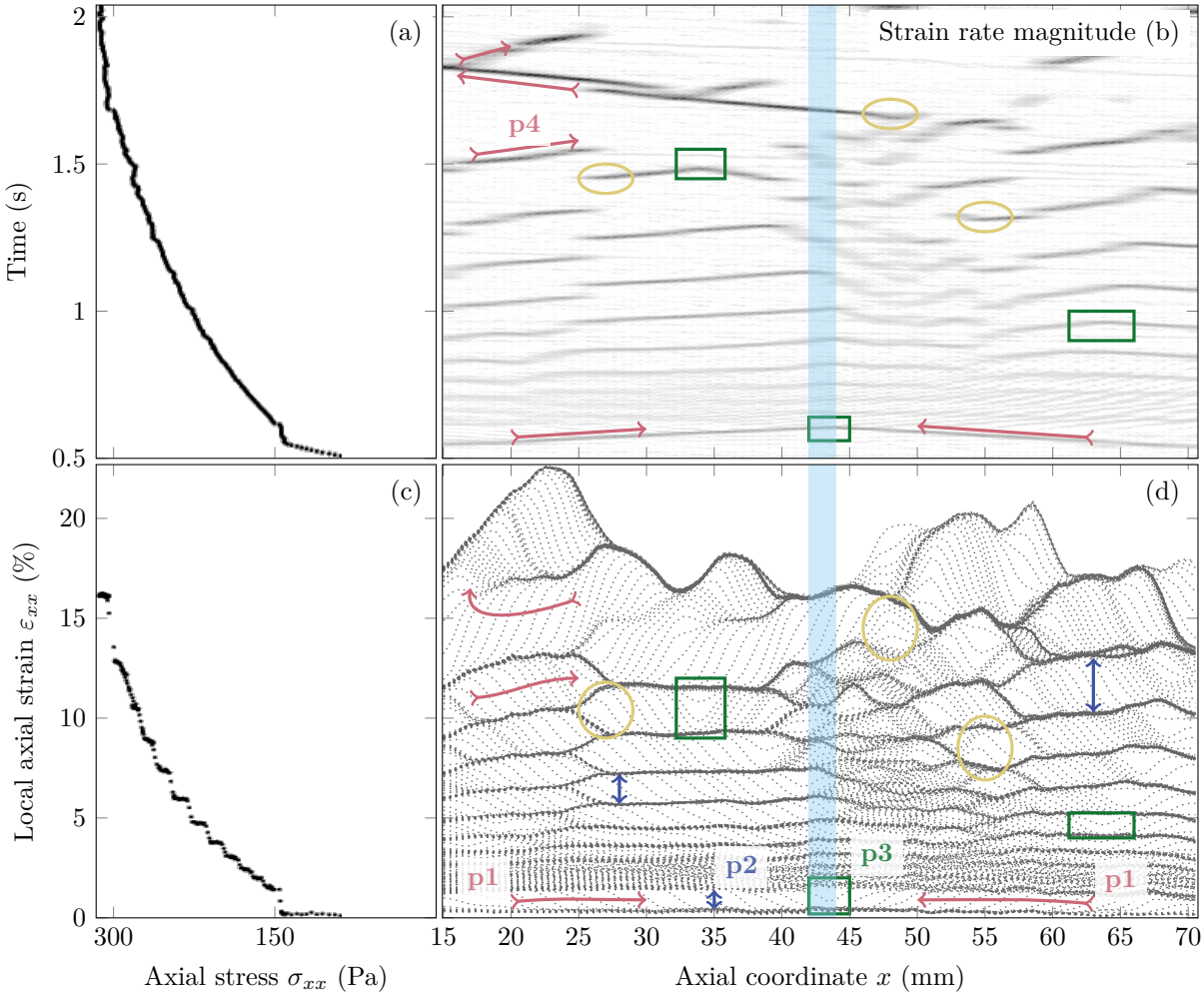

Figure 4: Results for large sample with a nominal strain rate of $10^{-1}\,\mathrm{s}^{-1}$. Figure 4a shows the evolution of stress vs. time. The time axis is in common with fig. 4b where the spatial distribution of strain rate is mapped at each instant—scalar values are normalized and range from 0 (white) to 1 (black). Figure 4c is the hardening curve where local strains are computed with a virtual gauge centered at $x = 43\,\mathrm{mm}$, shown here as highlighted zone ( ) on the right hand figures. Figure 4d displays the DIC axial strain measures in space at each captured instant. In figs. 4b and 4d, the common x axis is taken in the tensile direction and in the middle of the specimen. Drawings indicate locations in time and space corresponding to nucleations ( ), propagations ( ) and coalescences ( ); each can be found once on both figs. 4b and 4d. Finally, three strain increments are explicitly shown (blue arrows). Pointers are used in text references.

3. Results and discussion

3.1. Hardening

The stress-strain curves of six tensile tests are presented in fig. 5, which is divided into two graphs according to the geometry of the samples (small or large). Results are plotted as disconnected points to emphasize the sudden changes of ε_{xx}, which is arbitrarily measured in the middle of the sample over a single DIC element. NSRS is clearly observed since the average hardening values and serration amplitudes tend to increase with decreasing nominal strain rate.

The choice of strain measure has a decisive impact on the appearance and the clear representation of the consequent stress-strain behavior. By using a local strain measure, as opposed to global measures, we are able to obtain meaningful patterns. At low strains, a Lüders-like behavior is observed (fig. 5, zooms z1) after a yield limit of 145 MPa for most tests with an apparent continuity and no sudden stress drop, characteristic of the SSA contribution. Such a plateau is absent from two unique tests on small specimens above a nominal rate of $10^{-2}\,\mathrm{s}^{-1}$ where the yield stresses are 119.9 MPa and 115.7 MPa (fig. 5b and table 1a). This behavior may be due to a pre-strain of the small sample during the experimental setup. At the highest nominal strain rates, the PLC effect is reproduced in a progression of repeated steps (elastic loading followed by plastic plateaus) until fracture. For the lowest nominal strain rates, stress–strain curves show a grouping of points in steep clusters (more clearly visible as vertical segments in fig. 5, zooms z2) that correspond to reversible elastic-like loading paths. The highest point of each cluster corresponds to the start of a strain increment (horizontal void) correlated with a serration (vertical drop), which is the characteristic behavior of type B and C bands [38]. The serrations amplitude increase with decreasing nominal strain rate and increasing strain, up to 20 MPa. The specimen size does not appear to have any influence on stress drops amplitude (see section 3.5). This effect is illustrated onfig. 5 where the isolated point chosen to evaluate the strain is more rarely subjected to localization; the small samples produce clearer patterns because the associated points are more often found in the localized domain. Indeed, by reducing the sample area, a higher spatial resolution and a tighter zone of events allow an accurate evaluation of the mechanical state leading to a more exhaustive characterization of hardening.

Table 1a presents a quantitative summary of the work-hardening results where a single test of each nominal strain rate is arbitrarily chosen for the sake of clarity. The yield stress is taken at a strain of 0.5 %. The average stress–strain curves for both sets of samples remain consistent in spite of changes in geometry and apparatus.

The fracture strain of small specimens is systematically higher than that obtained for large samples which may be due to the presence of fewer defects induced by their smaller volume. As can be seen in fig. 5b, this essentially extends the necking phenomenon but does not cause a further spread of the PLC effect. This difference becomes much higher when the small samples are tested on Instron-10 kN than those tested on MicroTest-2 kN, which suggests that a bias is introduced by the change of machine. It can be due to configuration of MicroTest-2 kN which clamps are mounted on its frame and guided by a rail; whereas Instron-10 kN clamps allow lateral motion, hence lessen lateral stresses. Although this difference does not affect axial results, the more intense stresses due to MicroTest-2 kN transverse stiffness can lead to an earlier fracture.

3.2. Apparent propagation or temporal distribution

Figures 4b and 4d show a smooth wavelike propagation that, at first sight, would be observed for any test with nominal strain rates corresponding to type A or B. The characteristic representation

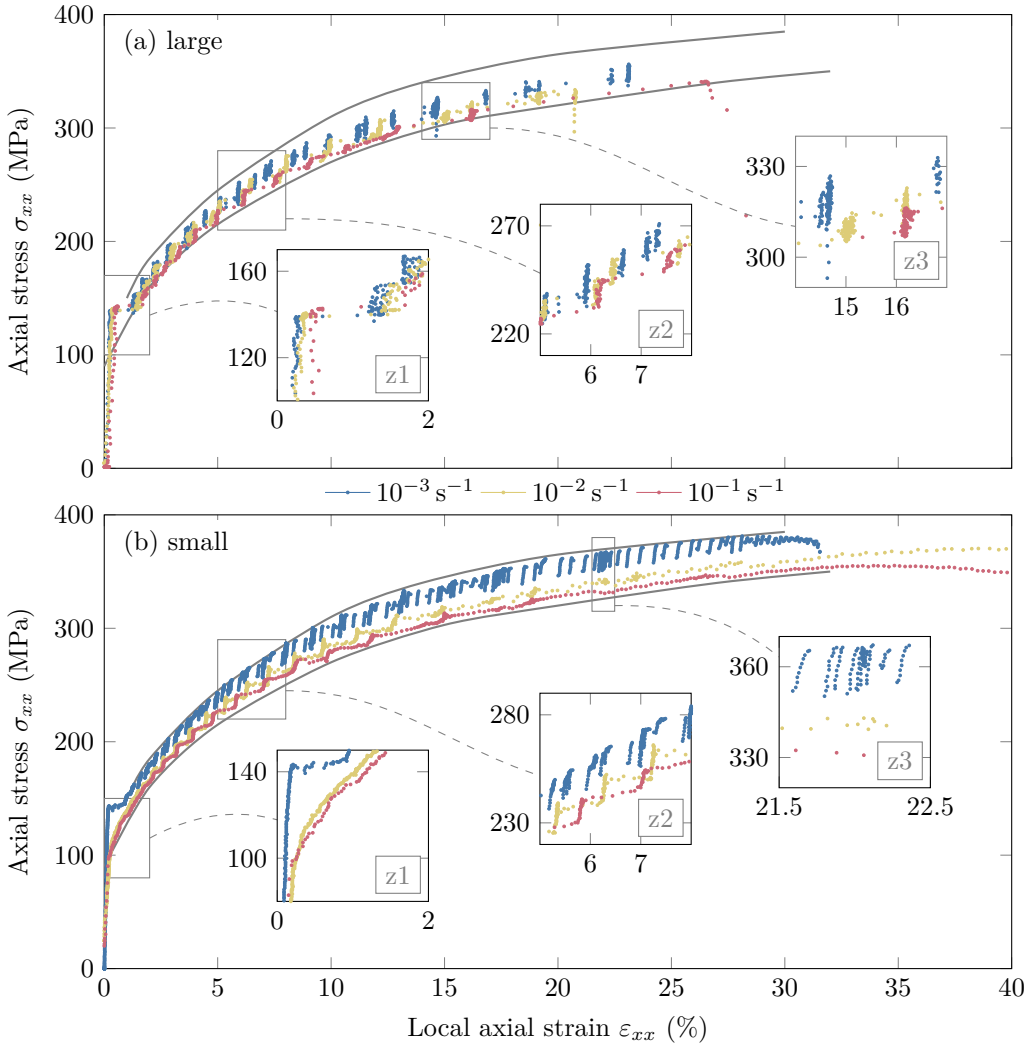

Figure 5: Cauchy stress vs. linearized Green–Lagrange strain curves on large (fig. 5a) and small (fig. 5b) samples, obtained with a DIC gauge located arbitrarily at the center of the specimens with the width of one finite element. Colors are associated with nominal strain rates specified in the legend. The same envelop curves are added to evaluate the influence of sample size on stress amplitudes.

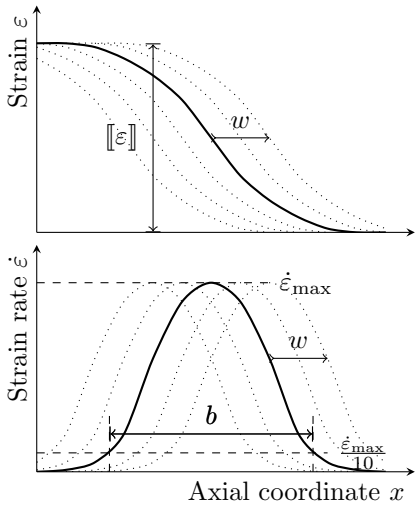

Figure 6: Schema for measurement of kinematic quantities: strain increment $[\![\varepsilon]\!]$, apparent band velocity w and band width b.

Geom.	Dev.	Nominal strain rate	Average strain rate	(a) Work-hard. (section 3.1)		(b) Bands widths (section 3.3)			
		v_c/L_c $10^{-3}\,\mathrm{s}^{-1}$	$\bar{v}/L$ $10^{-3}\,\mathrm{s}^{-1}$	σ_y MPa	ε^f_{xx} %	$\bar{b}^1_0$ mm	$\bar{b}^{10}_1$ mm	$\bar{b}^{20}_{10}$ mm	$\bar{b}^{30}_{20}$ mm
`large`	`Ins.`	0.1	0.1	139.3	25.7	2	2	2	2
		0.5	0.5	139.0	30.5	2.5	2.5	3	3
		1.0	1.1	138.3	35.5	4	4	4.5	4.5
		5.0	5.4	142.4	32.5	4.5	4.5	4.5	4.5
		10	10.9	139.2	35.3	5.5	5	5	5
		50	50.9	140.9	38.3	5 *	5	5	5
		100	89.2	142.7	38.4	5.5*	5 *	5 *	5.5
`small`	`Mic.`	0.2	0.1	147.6	38.2	2	2	2	2
		0.3	0.4	147.4	41.6	2	2	2	2
		0.7	1.0	143.2	40.9	2	2	2	2
`small`	`Ins.`	1.0	1.0	133.2	44.9	2	2	2	2
		10	9.3	119.9	64.7	2 *	2	2	2
		50	56.5	138.0	57.1	2 *	2	2	2
		100	152	115.7	71.0	2 *	2	2	2

Table 1: Quantitative summary of experiments. Geometry: large (`large`) or small (`small`) specimens. Device: Instron-10 kN (`Ins.`); MicroTest-2 kN (`Mic.`). Nominal strain rate v_c/L_c. The average strain rate $\bar{v}$ is the mean value of the measured gauge zone elongation rate v divided by the gauge zone length L. Work-hardening: yield stress σ_y and fracture strain ε^f_{xx}. Morphology: $\bar{b}^d_c$ is the averaged width (measured according to fig. 6) in the interval $\varepsilon_{xx} \in [c, d]$ in percents; $\bar{b}^1_0$ corresponds to PL bands while the rest are PLC. The marker (*) indicates the observation of two *coexisting* bands at several instants in the given strain range.

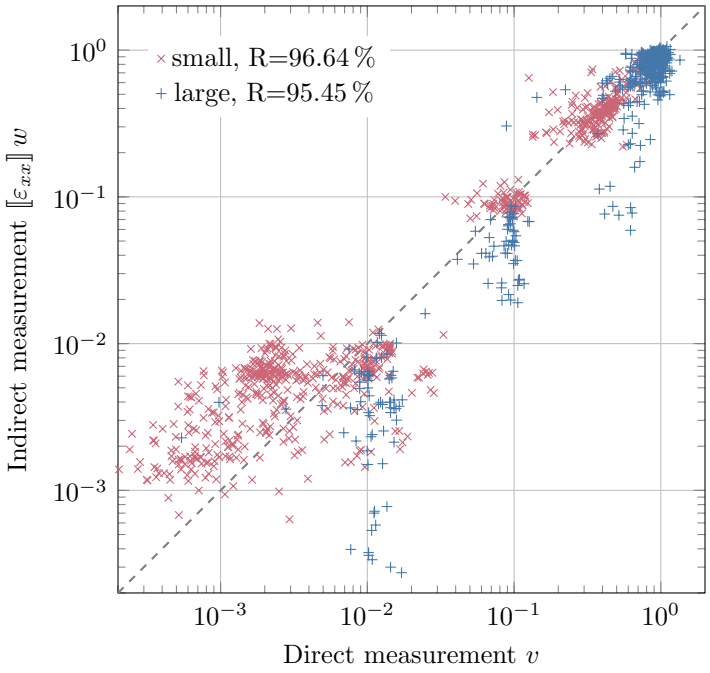

Figure 7: Gauge area elongation rate ($\mathrm{mm\,s^{-1}}$) for all results showing an apparent propagation—direct and indirect measurements are plotted with correlation coefficient R. Both direct and indirect measurements and prediction are obtained by post-treatment of the DIC results (see section 3.2).

(4b) allows us to measure subsequent bands locations (e.g. pointer p4) and hence compute an apparent wave velocity that was used by [27] to compare simulations with experimental results This propagating velocity has been estimated in several studies [20, 25, 27, 39, 40]. It is linked to the strain increment through a kinematic continuity condition [32]. According to the Hadamard [41] relation, the continuity of a weakly discontinuous displacement field expresses (here in the 1D tensile case):

$$v = [\![\varepsilon_{xx}]\!]\, w \tag{1}$$

where v is the gauge area elongation rate, $[\![\varepsilon_{xx}]\!]$ the axial strain increment (fig. 4d) and w the propagating velocity; they are illustrated on fig. 6. Thus, bands propagate as fast as necessary to accommodate the imposed kinematics. Therefore, an accurate description of the strain increment (see section 3.5) inherently results in a good description of the apparent propagation and vice versa.

The strain increments $[\![\varepsilon_{xx}]\!]$ (steps on fig. 4d) and associated bands locations (dark patterns on fig. 4b) are monitored using the characteristic and kinematic representations with a prediction algorithm prediction implemented with `Matlab`, which are then verified and corrected manually point-wise. The apparent bands velocities w are computed using polynomial approximations of the locations in time. The right-hand side ($[\![\varepsilon_{xx}]\!]\, w$) and the left-hand side (v) of eq. (1) are plotted in fig. 7 where strong correlation coefficients corroborate the above hypotheses and interpretation for both sample geometries. The indirect measurements deviations remain largely smaller than the orders of magnitude of the direct measurements. Indeed, they can be caused by post-treatment errors, by events occurring outside the gauge area or oscillations of the elongation rate.

Certain conceptual problems arise from considering PLC bands as slow plastic waves. First, it is incompatible with the observation of serrations since an oscillating flow is inherently correlated

with sudden kinematic changes: *true* propagation is frequently not smooth and the patterns of fig. 4b should be regarded as a finite collection of short horizontal segments rather than continuous lines. However, such an interpretation does not allow a unified characterization of the PLC effect since it is not be appropriate for describing type C kinematics that do not display propagating behaviors.

Because of the apparent propagating nature of the PLC effect at higher strain rates, the term band (in the singular) is often used to designate a volume within which the plastic strain rate suddenly increases, even when it travels over the material domain. In the present study, the term band refers to the individual event that takes place at a unique location. Therefore propagation is not taken into account and we consider rather the tendency of bands to nucleate side by side, even if they do so often enough to become indiscernible (type A). A propagating behavior is characterized here by subsequent nucleations that are spatially ordered.

Thus, a single description can be applied for both propagating (ordered) and non-propagating (disordered) behaviors. The property previously brought by the Hadamard relation is conserved and can be rephrased as follows: bands will nucleate as often as necessary to accomodate the imposed kinematics. Their global temporal behavior is adequately defined provided that there is an accurate description of the strain increment.

3.3. Morphology

The orientation of bands with respect to the tensile direction is assessed graphically on large samples strain rates maps. Small samples are excluded because of the shoulders proximity to any localization band. In accordance with previous studies [18, 12, 19, 21], the angle of orientation ranges between 55 and 65 degrees. As reported in [19], a shearing mode is systematically reported in the samples plane.

Using a method similar to [10], the width of bands is measured on the axial strain rate results: after identifying the strain rate peak (localization band), the width b is assessed graphically at 10 % of the peak height (see fig. 6). Results are presented is table 1b where the strain range of each test is divided into four intervals: $[0, 1]$ % for Lüders bands; then $[1, 10]$ %, $[10, 20]$ %, $[20, 30]$ % to distinguish PLC bands at the beginning, middle and end of the test, respectively. Each width value is the mean of ten measurements taken in the associated range, rounded to a precision of 0.5 mm due to the lack of precision of the peak shape, and oscillations of the signal at its edges. It should be noted that the widths are measured in the reference configuration and not transported to the current configuration.

On large samples, the band width is equal to 2 mm at the lowest nominal strain rates ($10^{-4}\,\mathrm{s}^{-1}$) and increases up to 5.5 mm at the highest rates ($10^{-1}\,\mathrm{s}^{-1}$). Such values are qualitatively consistent with previous studies [26, 32, 10, 21], suggesting a non linear monotonic increase of the bands widths with increasing strain rate. However, for small specimens and with the same method, this width is found to range from approximately 2 mm to 2.5 mm with no apparent sensitivity to rate and a higher level of confidence owing to the finer spatial resolution. Such a result has not yet been reported in the literature, and is further discussed in section 3.5.

3.4. Spatial distribution

To qualitatively assess the spatial distribution of localization bands, fig. 8 presents the kinematic representations of three different nominal strain rates (decreasing from top to bottom) applied to each of the two considered geometries (large in the left column and small in the right column). After a homogeneous increase of strain over the specimen, the first localization occurs for all samples

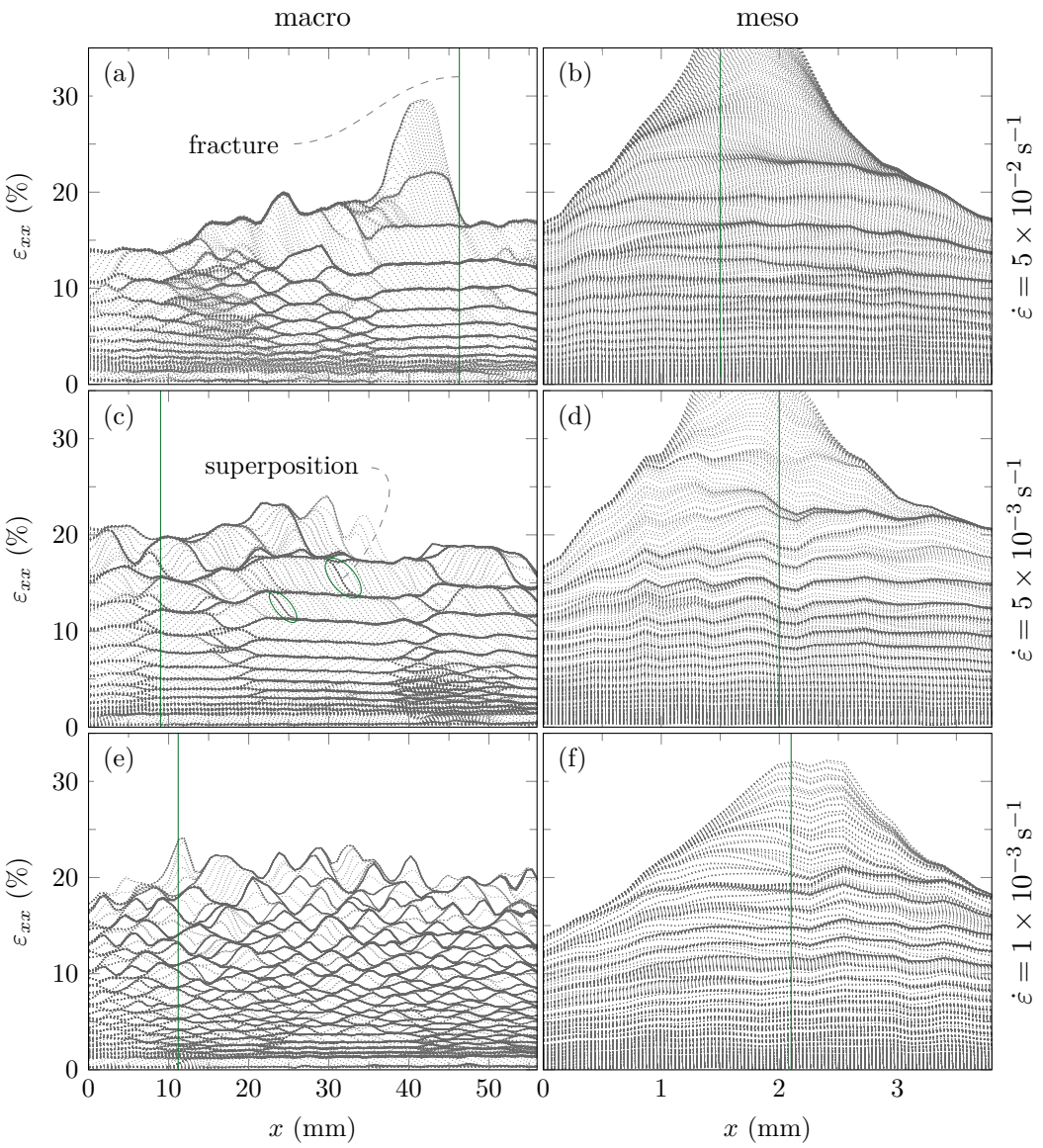

Figure 8: Subsequent strain states for different apparent strain rates plotted for both large (left column) and small (right column) samples. Each row corresponds to an order of magnitude of global strain rate specified on the right axis. Figures 8a and 8b (type A) as well as figs. 8c and 8d (type B) show spatially ordered patterns; while figs. 8e and 8f (type C) display a disordered behavior—see section 3.4. The fracture location is indicated with a vertical line.

at a common yield stress of 145 MPa. The location of the first band is due to local imperfections and can hardly be predicted. The subsequent bands (PL) follow a propagating pattern until full coverage of the gauge zone. The strain increment they carry is a consequence of SSA and remains at a value of 1.0(1) % independently of the applied velocity and irrespective geometry. The DSA mechanism starts at higher strains, with repeated occurrences of the PLC effect in different ways depending on the nominal strain rate of the test.

Figures 8a and 8b correspond to higher nominal strain rates and type A bands. The associated stress-strain curves are dominated by plateaus with a low number of serrations that are correlated with each first nucleation of an ordered set of bands. Nucleations are so frequent that they cannot be picked out in the DIC results. A clear propagating behavior is observed for most sets of bands, except in the annotated zone that corresponds, as mentioned in section 2.3, to the area with overlapping bands of opposite orientations. The second row (8c-8d) illustrates intermediate nominal strain rates corresponding to type B bands, where serrations become predominant. While the bands appear ordered in space as in type A, a kinematic difference can be observed in fig. 8c where intermittent persistent states are annotated. They reflect the hopping band trend associated with type B, expressed as a short break between two subsequent localizations which results in the superimposition of several measured strain states. This observation is consistent with the behaviors described in section 3.2: even though the propagating tendency (spatial order) is maintained, a lower imposed velocity implies a lower frequency of localization, rendering the events distinguishable. Figures 8e and 8f are associated with lower nominal strain rates and type C bands where serrations are larger in magnitude. In such regimes, the propagating patterns are frequently broken which result in an apparently disordered scheme. By contrast, only the large specimens (fig. 8e) clearly exhibit the characteristic disordered pattern of type C bands, while the small samples conserve a type B propagation trend in spite of an identical nominal strain rate and similar gauge area elongation rates (table 1).

The usual view of a "stochastic" or "random" distribution of bands that do not overlap [18] does not entirely cover what can be understood from the present experiments. Not only will two bands never nucleate successively at the same location, but type C bands tend to appear where the cumulative plasticity is minimal and thus follow an overall *deterministic* trend. As observed in classical plasticity, localization bands collectively tend to foster the homogeneity of strain. The kinematic trend becomes progressively ordered as the nominal strain rate increases—propagating patterns are first clearly observed at a nominal strain rate of $10^{-3}\,\mathrm{s}^{-1}$. From a macroscopic point of view, the tendency of bands to nucleate next to each other is influenced by the plastic strain gradient magnitude. Indeed, the steep strain step inherently produced by each band has for consequence a local peak of strain gradient that always matches the band location in the case of propagating behaviors (this can be seen from the simplified representation given on fig. 6). The gradient influence during plastic instabilities is in agreement with the strain gradient plasticity framework, applied by several authors to modeling the PLC effect [42, 43]. Consequently, the macroscopic spatial distribution of PLC bands can be seen as a competition between the minimal magnitude of plastic strain that dominates at lower strain rates, and the plastic strain gradient that takes over at higher strain rates. Since PL bands always appear at the onset of plasticity, their systematic propagation trend is caused by the plasticity gradient influence alone.

3.5. Characterization of transient states

The PLC effect involves a double-scale problem both in space (specimen length and band width) and in time (test duration and nucleation time). While the spatial issue is better addressed by

increasing images resolution, the acquisition frequency and quality are generally not high enough to accurately measure the kinetics of plastic instabilities during nucleation. Nevertheless, the localization effects can be characterized in terms of their outcome, by comparing initial and final states. Following this procedure, several studies have used the strain increment to characterize the consequence of a band [26, 22, 23, 25, 24, 27]. Using the kinematic representation, the difference of strain between initial and final states is measured at all possible instants on all of the tested specimens following the method described in section 3.2 (computer prediction and manual correction). In the case of disordered behaviors, the measurement is taken at the maximum increment, that is, in the middle of the band. The results are shown in fig. 9 as a function of the stress at nucleation time (peak value). A color bar indicates the instantaneous mean strain rate which is obtained from DIC results as the difference in velocity between the two edges of the gauge area. This method is applied to avoid the effects of geometry on the measured rates. A clearly consistent pattern can be noted because the scatter of points takes the form of a constitutive relation showing a monotonic evolution up to saturation associated with NSRS, which suggests that the strain increment is an intrinsic quantity that defines the action of a localization band. Even though the PL bands increment seems to be in continuity with the set of data points, it is always several times larger than the directly consecutive PLC bands. While such small values cannot be explicitly quantified, the difference can be readily observed on figs. 8a, 8c and 8e. A weak size effect is reported here since a strain increment scaling of $\sim 20\,\%$ is needed to achieve a quantitative match between the two distributions. In the literature, strain increments are usually reported as a function of cumulative plastic strain. The present results display the same NSRS when plotted as a function of the linearized Green–Lagrange measure. They agree with [27] where strain increments are measured using strain gauges, and a quasi-linear dependence is reported with cumulative plastic strain below $3\,\%$. Although strain increments have been reported to decrease with increasing strain rate [26] this was not observed in [22].

In fig. 10, the stress drops distributions are presented for each test as box plots shown as a function of the mean strain rate. Serrations are post-treated directly after the measurement and the data are maintained as such without further treatment; hence subjectivity is avoided but noise and small oscillations result in an overestimation of the amount of the smallest drops and a necessary shift of fractile values. The results are obtained following the method introduced by [9] for tensile tests, as reproduced experimentally in shear tests by [14] and numerically by [15]. In this approach, histograms are considered and characterized by the number of peaks and their location. In the present study, each corresponding histogram exhibits a single peak that tends to decrease with increasing strain rate, qualitatively matching with the results of [9]. The upper extreme and fractile values decrease exponentially with increasing strain rate, smoothly linking type C serrations to type A plateaus. The lower bounds can hardly be analyzed. A weak or negligible influence of the sample geometry is reported as regards the strain increment. This indicates that the stress drop is not only a structural response but an inherent actor in the nucleation process: since the stress drop is independent of size, its maximal amplitude can be predicted along with the strain increment knowing the mechanical state before nucleation.

The information on stress drops completes the kinematic observations which allows us to carry out the following analysis. Considering the one-dimensional problem of a rod of length L under constant imposed relative strain rate v/L; let τ be the nucleation time, i.e. the duration taken by a band to nucleate or the total time during which the plastic strain rate is non-zero. The increment

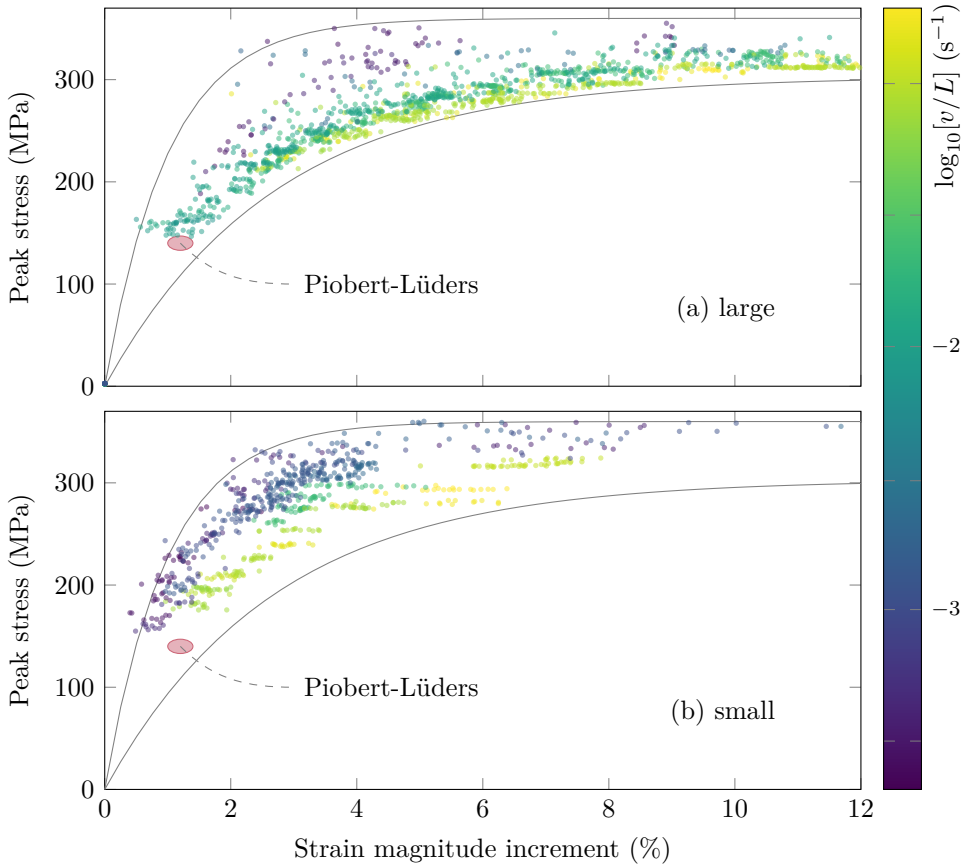

Figure 9: A constitutive relation at the scale of the localized zone. The strain magnitude increment is measured as illustrated in fig. 4. The stress measure is taken at the onset of localization, before its drop. Two identical envelope curves are added for comparison.

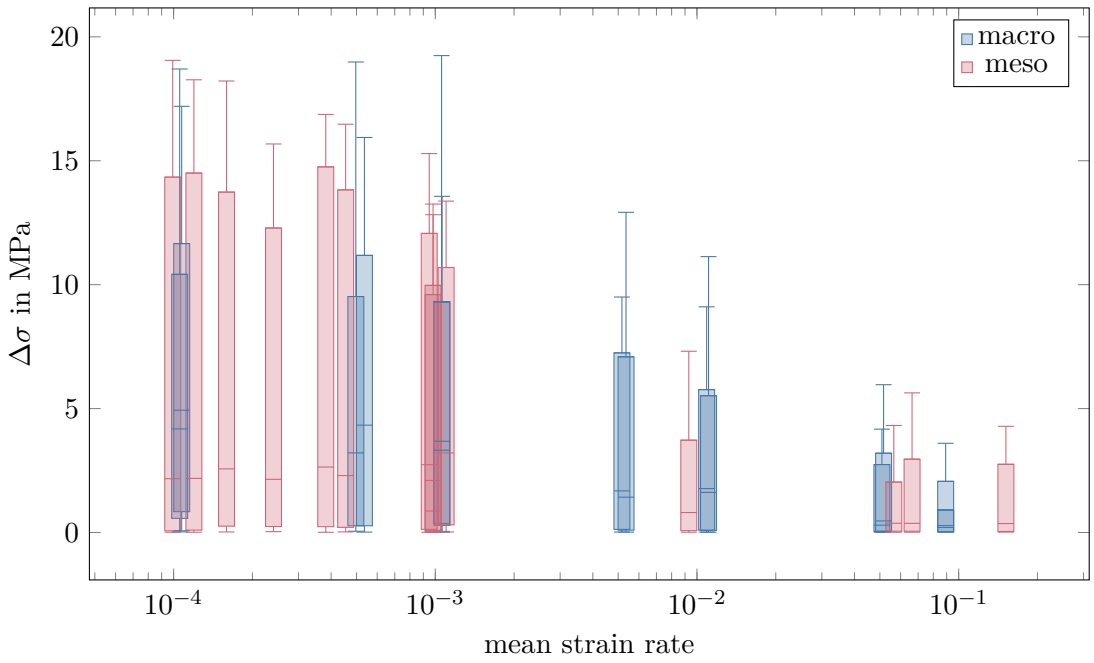

Figure 10: Box plot representation of serration distributions as a function of the averaged strain rate on the gauge area. Boxes delimit 5 % and 95 % fractiles; the segment inside each box is the median while whiskers indicates data extrema.

of length caused by a single nucleation can then be written

$$\Delta L = \int_\tau v \,\mathrm{d}t = \int_\tau \int_0^L (\dot\sigma/E + \dot\varepsilon^\mathrm{p})\,\mathrm{d}x\,\mathrm{d}t \tag{2}$$

$$\iff \quad v\tau = (\Delta\sigma/E)L + \Delta\varepsilon^\mathrm{p} b \tag{3}$$

where b is an equivalent band width. When the nominal strain rate is kept constant, increasing the length (in the present experiments from 4.2 mm to 60 mm) has no significant influence on $\{\Delta\sigma, \Delta\varepsilon^\mathrm{p}, b\}$ (resp. figs. 9 and 10 and section 3.3): in order to satisfiy eq. (3) the nucleation time τ accommodates size variations by decreasing with increasing length. This would imply that, during nucleation, the material constitutive relation thereof links strain differentials $\mathrm{d}\varepsilon^\mathrm{p}$ and stress differentials $\mathrm{d}\sigma$ with little or no implicit time dependence $\mathrm{d}t$. Indeed, the same results are obtained for $\Delta\sigma$ and $\Delta\varepsilon^\mathrm{p}$ with both geometries even though the nucleation process is several times faster for large samples. This postulate holds for both PL bands and the PLC effect. Moreover, the above feature allows us to understand the length effect measured in bands width (see section 3.3). Comparing small and large specimens at equal nominal strain rate, the wider bands observed in large specimen are in fact subjected to a higher instantaneous local strain rates arising from a shorter nucleation time. The commonly accepted concept of band width increasing with strain rate is thus validated and can partly explain the gauge length sensitivity. While experimental data does not argue against this explanation, a large increase in acquisition frequency and accuracy is required, as well as a more exhaustive set of length values, to provide empirical evidences and draw further conclusions.

Finally, table 1b indicates when two bands are observed simultaneously. Two PL bands are displayed at the same time in all large specimens tested with a nominal strain rate above $5 \times 10^{-3}\,\mathrm{s}^{-1}$,

and all small samples above $1 \times 10^{-3}\,s^{-1}$ (e.g. fig. 3). Two coexisting PLC bands are observed in all large specimens above $5 \times 10^{-2}\,s^{-1}$ (e.g. fig. 8a) at low strain levels, while never reported in small samples. The higher the strain rate, the longer the coexistence persists, and no more than two coexisting bands are ever displayed at any one time. These observations suggest the existence of a maximal local strain rate beyond which a band cannot grow, being lower for PL than for PLC bands. The fact that several PLC bands are never found in small samples is consistent with the above observation: a smaller length implies slower nucleations and a smaller associated strain rate. The coexistence of bands is often described in experimental studies, but no interpretations have been found in the literature.

4. Conclusion

The Portevin–Le Chatelier effect and Piobert–Lüders bands are investigated in an Al–Mg alloy at room temperature. A macroscopic interpretation is proposed which integrates the common discrete categories (A, B and C type bands) into a continuous description while distinguishing spatial (disordered and ordered trends, respectively driven by the plastic strain magnitude and its gradient) from temporal factors (nucleation frequency, extrinsic to the material behavior and governed by imposed kinematics). The key results of the present investigations are as follows.

i. Plastic strain increments are inherent to the nucleation of PL and PLC band. They are linked to stress at nucleation through a constitutive relation that expresses a negative strain rate sensitivity with no significant size sensitivity.
ii. The serrations distributions follow an overall decreasing trend with increasing strain rate and individual serrations show a monotonic increase with increasing strain. The development of serrations shows a small to negligible size sensitivity. Consequently, they can also be predicted without using transient differential equations.

Although the time refinement presented here does not exhaustively assess the nucleation process, a number of hypotheses are proposed by combining experimental evidence with a 1D kinematic model.

iii. The nucleation time and the strain rate carried by each band accommodate the size changes: the longer the sample, the faster the band evolution.
iv. There is an inherent limit to the bands strain rate, being lower for PL than for PLC bands, which explains the occurrence of several bands at the same time.

Acknowledgment

This research is supported by the Brittany region. The authors thank A. Jegat, A. Magueresse and H. Bellegou for their substantial involvement in the experimental investigations; and J. Réthoré for advice and permission to use his software [36]. M.S.N. Carpenter post-edited the English style and grammar.

Data availability

The raw/processed data required to reproduce these findings are available to download from `zenodo.org` [44].

References

[1] G. Piobert, Expérience sur la pénétration des projectiles dans le fer forgé, Mémoire de l'Artillerie (1842) 505.

[2] W. Lüders, Uber die ausserung der elasticitat an stahlartigen eisenstaben und stahlstaben, und uber eine beim biegen solcher stabe beobachtete molecularbewegung, Dingler's Polytechnisches Journal (fourth series) 5 (1860) 18–22.

[3] A. Le Chatelier, Influence du temps et de la température sur les essais au choc, Rev. Metall. / Cah. Inf. Tech. 6 (8) (1909) 914–917. doi:10.1051/metal/190906080914.

[4] A. Portevin, F. Le Chatelier, Sur un phénomène observé lors de l'essai de traction d'alliages en cours de transformation (1923).
URL http://gallica.bnf.fr/ark:/12148/bpt6k3086n

[5] A. H. Cottrell, B. A. Bilby, Dislocation theory of yielding and strain ageing of iron, Proc. Phys. Soc. London, Sect. A 62 (1) (1949) 49. doi:10.1088/0370-1298/62/1/308.

[6] A. van den Beukel, Theory of the effect of dynamic strain aging on mechanical properties, Phys. Status Solidi A 30 (1) (1975) 197–206. doi:10.1002/pssa.2210300120.

[7] P. G. McCormick, Theory of flow localisation due to dynamic strain ageing, Acta Metall. 36 (12) (1988) 3061–3067. doi:10.1016/0001-6160(88)90043-0.

[8] S. D. Antolovich, R. W. Armstrong, Plastic strain localization in metals: origins and consequences, Prog. Mater Sci. 59 (2014) 1–160. doi:10.1016/j.pmatsci.2013.06.001.

[9] M. Lebyodkin, L. Dunin-Barkowskii, Y. Brechet, Y. Estrin, L. P. Kubin, Spatio-temporal dynamics of the Portevin-Le Chatelier effect: experiment and modelling, Acta Mater. 48 (10) (2000) 2529–2541. doi:10.1016/s1359-6454(00)00067-7.

[10] H. Ait-Amokhtar, P. Vacher, S. Boudrahem, Kinematics fields and spatial activity of Portevin-Le Chatelier bands using the digital image correlation method, Acta Mater. 54 (16) (2006) 4365–4371. doi:10.1016/j.actamat.2006.05.028.

[11] F. Chmelík, A. Ziegenbein, H. Neuhäuser, P. Lukáč, Investigating the Portevin–Le Châtelier effect by the acoustic emission and laser extensometry techniques, Mater. Sci. Eng., A 324 (1-2) (2002) 200–207. doi:10.1016/s0921-5093(01)01312-0.

[12] J. Zdunek, T. Brynk, J. Mizera, Z. Pakieła, K. J. Kurzydłowski, Digital image correlation investigation of Portevin–Le Châtelier effect in an aluminium alloy, Mater. Charact. 59 (10) (2008) 1429–1433. doi:10.1016/j.matchar.2008.01.004.

[13] A. Yilmaz, The Portevin-Le Chatelier effect: a review of experimental findings, Sci. Technol. Adv. Mater. 12 (6) (2011) 063001. doi:10.1088/1468-6996/12/6/063001.

[14] J. Coër, P.-Y. Manach, H. Laurent, M. C. Oliveira, L. F. Menezes, Piobert-Lüders plateau and Portevin-Le Chatelier effect in an Al-Mg alloy in simple shear, Mech. Res. Commun. 48 (2013) 1–7. doi:10.1016/j.mechrescom.2012.11.008.

[15] P.-Y. Manach, S. Thuillier, J. W. Yoon, J. Coër, H. Laurent, Kinematics of Portevin-Le Chatelier bands in simple shear, Int. J. Plast. 58 (2014) 66–83. doi:10.1016/j.ijplas.2014.02.005.

[16] J. Min, L. G. Hector, J. E. Carsley, T. B. Stoughton, B. E. Carlson, J. Lin, Spatio-temporal characteristics of plastic instability in AA5182-O during biaxial deformation, Mater. Des. 83 (2015) 786–794. doi:https://doi.org/10.1016/j.matdes.2015.06.039.

[17] J.-B. L. Cam, E. Robin, L. Leotoing, D. Guines, Calorimetric analysis of Portevin-Le Chatelier bands under equibiaxial loading conditions in Al-Mg alloys: kinematics and mechanical dissipation, Mech. Mater. 105 (2017) 80–88. doi:10.1016/j.mechmat.2016.11.012.

[18] K. Chihab, Y. Estrin, L. P. Kubin, J. Vergnol, The kinetics of the Portevin–Le Châtelier bands in an Al-5at% Mg alloy, Scr. Metall. 21 (2) (1987) 203–208. doi:10.1016/0036-9748(87)90435-2.

[19] Y. L. Cai, S. L. Yang, Y. H. Wang, S. H. Fu, Q. C. Zhang, Characterization of the deformation behaviors associated with the serrated flow of a 5456 Al-based alloy using two orthogonal digital image correlation systems, Mater. Sci. Eng., A 664 (2016) 155–164. doi:10.1016/j.msea.2016.04.003.

[20] H. Ait-Amokhtar, C. Fressengeas, S. Boudrahem, The dynamics of Portevin–Le Chatelier bands in an Al-Mg alloy from infrared thermography, Mater. Sci. Eng., A 488 (1) (2008) 540–546. doi:10.1016/j.msea.2007.11.075.

[21] D. Yuzbekova, A. Mogucheva, D. Zhemchuzhnikova, T. Lebedkina, M. Lebyodkin, R. Kaibyshev, Effect of microstructure on continuous propagation of the Portevin-Le Chatelier deformation bands, Int. J. Plast. 96 (2017) 210–226. doi:10.1016/j.ijplas.2017.05.004.

[22] Z. Kovács, J. Lendvai, G. Vörös, Localized deformation bands in Portevin–Le Châtelier plastic instabili-

ties at a constant stress rate, Mater. Sci. Eng., A 279 (1) (2000) 179–184. doi:https://doi.org/10.1016/S0921-5093(99)00628-0.

[23] K. Renard, S. Ryelandt, P. J. Jacques, Characterisation of the Portevin–Le Châtelier effect affecting an austenitic TWIP steel based on digital image correlation, Mater. Sci. Eng., A 527 (12) (2010) 2969–2977. doi:https://doi.org/10.1016/j.msea.2010.01.037.

[24] J. Min, J. Lin, B. Sun, Effect of strain rate on spatio-temporal behavior of Portevin–Le Châtelier bands in a twinning induced plasticity steel, Mech. Mater. 68 (2014) 164–175. doi:https://doi.org/10.1016/j.mechmat.2013.09.002.

[25] C. Bernard, J. Coër, H. Laurent, P. Chauvelon, P. Y. Manach, Relationship between local strain jumps and temperature bursts due to the Portevin-Le Chatelier effect in an Al-Mg alloy, Exp. Mech. 53 (6) (2013) 1025–1032. doi:10.1007/s11340-012-9711-4.

[26] A. Ziegenbein, P. Hähner, H. Neuhäuser, Correlation of temporal instabilities and spatial localization during Portevin–Le Châtelier deformation of Cu–10 at.% Al and Cu–15 at.% Al, Comput. Mater. Sci. 19 (1) (2000) 27–34. doi:10.1016/S0927-0256(00)00136-1.

[27] B. Klusemann, G. Fischer, T. Böhlke, B. Svendsen, Thermomechanical characterization of Portevin-Le Châtelier bands in AlMg3 (AA5754) and modeling based on a modified Estrin-McCormick approach, Int. J. Plast. 67 (2015) 192–216. doi:10.1016/j.ijplas.2014.10.011.

[28] M. Abbadi, P. Hähner, A. Zeghloul, On the characteristics of Portevin-Le Chatelier bands in aluminum alloy 5182 under stress-controlled and strain-controlled tensile testing, Mater. Sci. Eng., A 337 (1) (2002) 194–201. doi:10.1016/s0921-5093(02)00036-9.

[29] H. Louche, P. Vacher, R. Arrieux, Thermal observations associated with the Portevin-Le Châtelier effect in an Al-Mg alloy, Mater. Sci. Eng., A 404 (1-2) (2005) 188–196. doi:10.1016/j.msea.2005.05.058.

[30] A. Benallal, T. Berstad, T. Børvik, O. S. Hopperstad, I. Koutiri, R. Nogueira De Codes, An experimental and numerical investigation of the behaviour of AA5083 aluminium alloy in presence of the Portevin-Le Chatelier effect, Int. J. Plast. 24 (10) (2008) 1916–1945. doi:10.1016/j.ijplas.2008.03.008.

[31] N. Ranc, W. Du, I. Ranc, D. Wagner, Experimental studies of Portevin-Le Chatelier plastic instabilities in carbon-manganese steels by infrared pyrometry, Mater. Sci. Eng., A 663 (2016) 166–173. doi:https://doi.org/10.1016/j.msea.2016.03.096.

[32] P. Hähner, A. Ziegenbein, E. Rizzi, H. Neuhäuser, Spatiotemporal analysis of Portevin–Le Châtelier deformation bands: theory, simulation, and experiment, Phys. Rev. B 65 (2002) 134109. doi:10.1103/PhysRevB.65.134109.

[33] P.-Y. Manach, H. Laurent, J. Coër, Benchmark 3 Numisheet 2016, https://www.researchgate.net/project/Benchmark-3-Numisheet-2016, accessed: 2018-02-22 (2016).
URL https://www.researchgate.net/project/Benchmark-3-Numisheet-2016

[34] R. Hielscher, H. Schaeben, A novel pole figure inversion method: specification of the *mtex* algorithm, J. Appl. Crystallogr. 41 (6) (2008) 1024–1037. doi:10.1107/S0021889808030112.

[35] X. Feng, G. Fischer, R. Zielke, B. Svendsen, W. Tillmann, Investigation of PLC band nucleation in AA5754, Mater. Sci. Eng., A 539 (2012) 205–210. doi:10.1016/j.msea.2012.01.082.

[36] J. Réthoré, UFreckles (Oct. 2018). doi:10.5281/zenodo.1433776.

[37] M. Mazière, J. Besson, S. Forest, B. Tanguy, H. Chalons, F. Vogel, Numerical aspects in the finite element simulation of the Portevin-Le Chatelier effect, Comput. Meth. Appl. Mech. Eng. 199 (9) (2010) 734–754. doi:10.1016/j.cma.2009.11.004.

[38] K. Chihab, L. P. Kubin, Héterogéneités macroscopiques de la plasticité de type sensibilite negative a la vitesse de deformation, Sci. Tech. A.

[39] A. Benallal, T. Berstad, T. Børvik, A. H. Clausen, O. S. Hopperstad, Dynamic strain aging and related instabilities: experimental, theoretical and numerical aspects, Eur. J. Mech. A. Solids 25 (3) (2006) 397–424. doi:10.1016/j.euromechsol.2005.10.007.

[40] X. G. Wang, L. Wang, M. X. Huang, Kinematic and thermal characteristics of Lüders and Portevin-Le Châtelier bands in a medium Mn transformation-induced plasticity steel, Acta Mater. 124 (2017) 17–29. doi:10.1016/j.actamat.2016.10.069.

[41] J. Hadamard, Leçons sur la propagation des ondes et les équations de l'hydrodynamique, Cours du collège de France, Librairie scientifique A. Hermann, Paris, 1903.

[42] H. M. Zbib, E. C. Aifantis, A gradient-dependent model for the Portevin–Le Châtelier effect, Scr. Metall. 22 (8) (1988) 1331–1336. doi:10.1016/S0036-9748(88)80157-1.

[43] M. Mazière, S. Forest, Strain gradient plasticity modeling and finite element simulation of Lüders band formation and propagation, Continuum Mech. Thermodyn. 27 (1-2) (2013) 83–104. doi:10.1007/s00161-013-0331-8.

[44] B. Reyne, P.-Y. Manach, A. Jegat, A. Magueresse, H. Bellegou, AA5086 characterization in tension at several

constant strain rates and room temperature using DIC with occurence of the Portevin–Le Chatelier effect, Zenodo research data repository, open access (Oct. 2017). doi:10.5281/zenodo.1312836.